IET Image Processing

Research Article

Quantitative analysis of cell morphology based on the contourlet transform

ISSN 1751-9659
Received on 22nd July 2019
Revised 31st March 2020
Accepted on 1st May 2020
E-First on 8th September 2020
doi: 10.1049/iet-ipr.2019.0909
www.ietdl.org

Yali Huang[1]*, Xuefang Hu*[1]*, Lei Hao*[1]*, Yuehua Gao*[1]*, Zhiwen Liu*[2]*, Peiguang Wang*[1] ✉
[1]*College of Electronic Information Engineering, Hebei University, Baoding, 071002, People's Republic of China*
[2]*School of Information and Electronics, Beijing Institute of Technology, Beijing, 100081, People's Republic of China*
✉ *E-mail: pgwang@hbu.edu.cn*

Abstract: Cellular morphology analysis has been widely used to detect abnormalities in biological processes. Clinicians have observed that lymphocytes become highly deformable under special conditions, particularly when graft rejection occurs. The characterisation of lymphocyte boundary deformation provides important quantitative parameters to assist clinical rejection diagnosis. To evaluate the dynamic features of the boundaries of target lymphocyte when a graft rejection occurs, a contourlet transform-based method is proposed to extract the characteristics of cell boundary variation. First, the lymphocyte is segmented and tracked to obtain their edge-to-centroid distance signals. Subsequently, a contourlet transform is performed on these signals, during which the edge-to-centroid distance signals of the lymphocyte is decomposed at multiple scales using the Laplacian pyramid; a multi-directional decomposition is then performed using a direction filter to merge the singularities distributed along the same direction and obtain the contourlet transform coefficients. Finally, statistical parameters of the cell dynamic boundaries are calculated, then fed into the support vector machine for classification of the cell deformation. Our findings demonstrate that contourlet transform has better performance in representing image features such as cell boundaries than wavelet transform for its prosperities of multi-scale and multi-directional decomposition for cell images.

1 Introduction

The cell is the basic structural and functional unit of an organism, change of which reflects the physiological and pathological characteristics of the living body. Analysing the morphological changes of a target cell in microscopic images allows one to access the metabolic information of living organisms [1–3]. The analysis of cell morphology has been extensively used in clinical diagnosis and biological research, including inflammation, wound healing, drug verification, early cancer diagnosis, tumour therapy, and immune response [4–7].

The traditional analysis of cell morphology requires the doctor to observe and identify the cell visually through a microscope and provide diagnostic results by comparing the observation against a micrograph. Consequently, diagnostic results can be subjective depending on the level of experience of the doctor. In contrast, feature extraction and pattern recognition have been widely used in the field of medical image analysis to provide objective and quantitative feature parameters for detecting cell features and to assist with clinical diagnoses [8–10].

Many applications of cell image analysis have been developed in previous years, including cell classification, segmentation and tracking, and quantitative analysis of cell deformation [7, 11–13]. Chen *et al*. reported that analysis of cell morphology has made a particularly significant contribution to the diagnosis of diseases, and attracted widespread attention [14]. An *et al*. conducted studies on morphological feature extraction and pattern classification in cell images [15]. Huang *et al*. compared different methods of describing cell morphologies and conducted a quantitative analysis of dynamic images of the cells that could be used for rapid clinical rejection diagnosis [16].

Characterising an image edge is an important prerequisite for cell deformation research [13]. Typical edge feature extraction algorithms include differential edge extraction, morphological edge extraction, edge extraction combined with image error analysis, and wavelet transform. Among them, the wavelet transform method can capture the singularities of a one-dimensional signal and achieve an ‘optimal’ non-linear approximation by virtue of its intrinsic multi-scale characteristics [17]. However, wavelet transform cannot provide optimal representations of the singularities in a curve or a surface in two or more dimensions [18]. Considering that signals with a ‘line or surface’ singularity are very common in high-dimensional space, in reality, the desired algorithm should be able to detect, represent, and deal with data in high-dimensional spaces and provide an optimum representation of high-dimensional functions containing curves or surfaces with singularities. To this aim, Do and Vetterli proposed the contourlet transform, also known as pyramidal directional filter bank (DFB), which decomposes an image at any scale and in any direction [19]. This feature allows it to yield an effective representation of a smooth contour, which is a very common feature in natural images, as well as a sparser representation of the lines and surface in the image.

The contourlet transform can effectively capture the intrinsic contours and edges in natural images for its multi-scale and multi-direction properties. It has been widely used in image denoising [20, 21], image enhancement [22, 23], image fusion [24, 25], and image segmentation [26, 27]. Asmare *et al*. reported that the contourlet method captured the closest profile to the perfect image [23]. Sathya *et al*. demonstrated that contourlet coefficients obtained via the contourlet transform exhibited better performance in enhancing the vessel-like segments than the wavelets with its anisotropy and directionality characteristics [27]. This literature dictates that contourlet transform exhibits better performance in representing the image salient features such as edges, lines, curves, and contours than wavelets for its anisotropy and directionality and is therefore well suited for multi-scale edge-based image feature extraction and pattern recognition [28].

In this study, first, the contourlet transform and wavelet transform are both performed on the two-dimensional plane curves of the edge-to-centroid distance signals from cell boundaries. Second, quantitative statistical parameters are calculated effectively from the sub-band coefficients in the transformation domain, and the rank-sum test is performed to find the feature vector, which can best characterise cell deformation. Lastly, the feature vector is fed into the neural network for the classification of the two kinds of cell deformation.

The remaining paper is organised as follows. Materials and methods are introduced in Section 2, followed by results in Section 3. Finally, discussions and conclusions are provided in Section 4.

2 Materials and methods

2.1 Materials

The cell image sequences were acquired by an optical phase contrast microscope at a magnification of 16,000× from the peripheral blood samples of clean healthy mice 7 days after the skin transplantation. The mice in our experiments are 6–8 weeks and 20–22 g. Experiments ensure that there is only one object-lymphocyte in each frame image. That is to say, we only observe one lymphocyte in each frame of the image. The animal experiments were conducted by the trained staff in Beijing You'an Hospital, which is affiliated to the Capital Medical University. Also, the hospital is a Grade-III Class-A hospital of the Ministry of Health in China. All the disposals are in accordance with the guideline of animal ethics. Two kinds of experiments were conducted. The first experiment was implemented through autologous transplantation. Healthy Balb/C male mice were used as both hosts and donors; this was the self-skin transplantation (SST) group. The second experiment was implemented through allogenic transplantation, in which healthy Balb/C male mice were used as hosts while healthy C57BL/6 male mice were used as donors; this was the allogenic skin transplantation (AST) group.

The shape of the lymphocyte is stable, and the deformation is slight in the SST group. There is no acute rejection in this case, which is a normal group. The lymphocytes are more active, and the deformation is intense in the AST group. There is acute rejection in this case, which is recalled in an abnormal group.

40 videos (each ∼20–30 s in duration) of peripheral immune blood cells of mice were chosen for the study. Half of the videos were taken from the SST group, and the other half were taken from the AST group. It should be noted that cell boundaries were segmented and tracked using our previous method prior to the quantitative analysis of cell boundary changes [29].

2.2 Wavelet transform

The wavelet transform exhibits a flexible ‘time-frequency’ window and is, therefore, an ideal tool for performing time-frequency localisation analysis. In other words, when the window area (size) is given, its shape changes with varying levels of the localised frequency in signal [17]. When analysing the high-frequency component of the signal, the time window is automatically narrowed, and the frequency window is automatically widened; in contrast, when analysing the low-frequency component of the signal, the time window is automatically widened, and the frequency window is automatically narrowed. The expression of the wavelet transform is given by

$$\mathrm{WT}_x(a,b) = \frac{1}{\sqrt{a}}\int_{-\infty}^{+\infty} x(t)\varphi^*\left(\frac{t-b}{a}\right)\mathrm{d}t \tag{1}$$

where $x(t)$ is the original input signal to be transformed; $\varphi(t)$ is the basis function (mother wavelet) of wavelet transform; ‘*’ represents the conjugation of the functions; a represents the time axis scaling parameter and b is the time-lapse parameter. The coefficient $1/\sqrt{a}$ is a scale normalisation factor that ensures wavelets of different scales possess the same amount of energy.

Stretching and translating the mother wavelet yields a family of basic function: $\varphi_{a,b}(t) = (1/\sqrt{a})\varphi((t-b)/a)$. When a increases, the corresponding wavelet function $\varphi_{a,b}(t)$ widens along the time axis and vice versa. Fig. 1 shows the schematic of the change in the time-frequency window of the wavelet transform. The green rectangle represents the time-frequency window of the mother wavelet. The red rectangle indicates the condition when a decreases and the time-frequency window becomes narrower. In this case, the centre frequency is automatically adjusted to the higher part of the frequency axis, similar to high-frequency analysis of signals using the narrow window. The blue rectangle indicates the condition when a increases and the time-frequency window widens, in which the centre frequency is automatically adjusted to the lower part of the frequency axis, similar to low-frequency analysis of signals using the wide window.

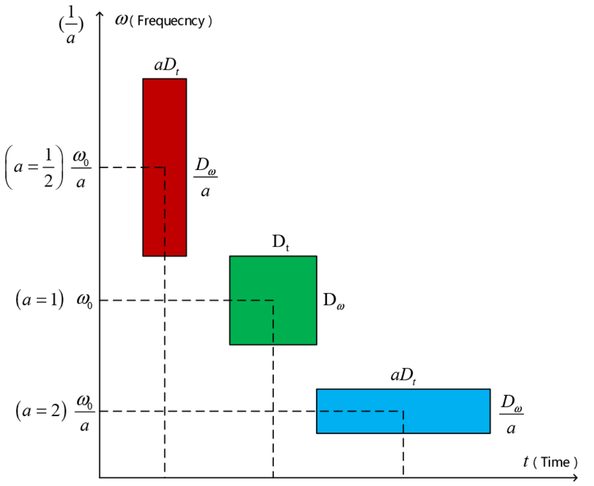

Fig. 1 *Schematic of change in time-frequency window of the wavelet transform*

When analysing two-dimensional or higher-dimensional signals, the wavelet transform cannot utilise the unique geometric properties of the data effectively [19]. Consequently, it fails to represent the signal with the optimal or most sparse function.

2.3 Contourlet transform

To detect and represent data in high-dimensional space, the contourlet transform, known as multi-scale geometric analysis, was proposed to provide optimal representations of high-dimensional functions independently in different disciplines [19, 30, 31]. Such a transformation can represent two-dimensional images with multi-resolution analysis, local positioning, and multi-directionality.

In the contourlet transform, a basic structure similar to that of the contour segment is used to approximate the image. This basic structure is a strip structure with an aspect ratio that varies with the scale. This approach can realise the decomposition of the image at any scale and in any direction, as opposed to the wavelet transform, which can only perform decomposition in three directions (horizontal, vertical, and diagonal). Additionally, the contourlet transform can provide a sparser representation of the lines and surfaces in the image while better delineating contours and directional textures.

The contourlet transform is performed in two steps. First, the Laplacian pyramid (LP) transformation is applied to decompose the input image into high-frequency and low-frequency sub-bands to ‘capture’ the singularities. Second, a DFB is used to further decompose the high-frequency and low-frequency sub-bands into multi-directional sub-bands and merge the singularities distributed along the same direction into a single coefficient, which is defined as the contourlet transform coefficient.

Let F be a bounded linear functional on the Hilbert space H [32]. According to the Riesz representation theorem, a unique $x_0 \in H$ exists such that for any $x \in H$, and we have $F(x) = \langle x, x_0\rangle$. $F(x)$ represents different transforms when different basic functions x_0 are used. If x_0 represents the basic function system R^M in the LP filter coefficients space, denoting the function as $\{\phi_j\}_{j=0}^{M-1}$ and the input signal as $\boldsymbol{x}$, then the LP decomposition can be expressed as an inner product form as follows [19]:

$$s_j = \langle \boldsymbol{x}, \phi_j\rangle \tag{2}$$

Similarly, the operation of the DFB on the sub-band image can be expressed as follows:

$$t_k = \langle \boldsymbol{x}, \varphi_k\rangle \tag{3}$$

where $\{\varphi_k\}_{k=0}^{N-1}$ is the basic function system $R^N(N = 0, \ldots, 2^l - 1)$ in the DFB space. In other words, there are 2^l sub-bands after multi-directional decomposition.

According to (2) and (3), the inner product expression of the contourlet transform is given as follows:

$$c_{j,k} = \langle\langle \boldsymbol{x}, \phi_j\rangle, \varphi_k\rangle = \langle \boldsymbol{x}, \langle\phi_j, \varphi_k\rangle\rangle = \langle \boldsymbol{x}, \beta_{j,k}\rangle \tag{4}$$

where $\beta_{j,k}$ is the basis of the transformation space, $R^{M\times N}$ and $c_{j,k}$ are the coefficients after the contourlet transform [19].

2.4 Comparison of the contourlet transform with the wavelet transform

To compare the effectiveness of the contourlet and wavelet transform, two-step contourlet and wavelet transforms are performed on the Facetscol image. The results from the transformations are shown in Figs. 2*a* and *b*. During the contourlet transform, the original image is decomposed into sub-bands in four directions in the first step and eight directions in the second step. The coefficients of each sub-band represent features of the signal along with different directions, with the larger and smaller coefficients corresponding to the brighter and darker locations, respectively.

It can be seen that the wavelet transform can only perform decomposition in three directions (horizontal, vertical, and diagonal) at each scale. While the contourlet transform can capture edge features in more directions. The approximation of the singular line in the image using the wavelet transform is accomplished by the supportive section with square shapes. In other words, the 'line' is approximated by the 'point.' Therefore, when decomposing the image with a multi-level scale, many non-trivial coefficients appear, ultimately leading to poor representation of the original function. While the contourlet transform provides a sparse representation for two-dimensional piecewise smooth signals resembling images, which is realised by supportive sections with rectangular shapes. As a rectangular supportive section represents the directional dependence—an anisotropic feature—it is more advantageous for expressing small directional contours and line segments in the image.

Furthermore, the contourlet transform is reversible because both LP decomposition and DFBs exhibit refactoring properties. Therefore the contourlet transform coefficients can be used to reconstruct the original image completely. Figs. 3*a* and *b* show the original Facetscol image and the image reconstructed from the inverse of the contourlet transform, respectively.

2.5 Proposed method

In this study, the boundary of the target cell in the microscopic video is a closed and smooth contour curve in two-dimensional space. We first segmented and tracked the boundaries of the target cell, then calculated the corresponding edge-to-centroid distance signals.

The edge-to-centroid distance signals of the target cell in the video are obtained from cell boundaries as shown in Fig. 4. First, 256 frames are obtained from 512 consecutive frames in the video by sampling at the interval of 2, as shown in Fig. 4*a*. The target cell is then tracked and segmented to obtain their boundaries based on our previous approach [29], as shown in Fig. 4*b*. Second, the pixels are interpolated on the boundary, making sure that there are 256 sampling points on the boundary of each target cell. That is to say, each video includes 256 frames after sampling, and the cell boundary in each frame contains 256 sampling points. After that, the edge-to-centroid distance signals are obtained by calculating the distance from each sampling point on the cell boundary to the centroid of the cell.

The edge-to-centroid distance signals are denoted as $r(p, t)$, where $p = 1, 2, 3, \ldots, 256$ represents the sampling points on the boundary and $t = 1, 2, 3, \ldots, 256$ represents the temporal points over time, then the value of $r(p, t)$ represents the edge-to-centroid distance from the sampling point p on the boundary at time t to the cell centroid. If we place the signal $r(p, t)$ in a three-dimensional space and link p, t, r to x, y, z axes, respectively, then the change of r along the x-axis represents the spatial change of the cell boundary; whereas the change of r along the y-axis represents the temporal change of the cell boundary. Spreading out all the edge-to-centroid distance signals in three-dimensional space yields a surface signal, as shown in Fig. 4*c*.

After that, the wavelet and contourlet transforms were performed on the above edge-to-centroid distance signals. To quantitatively analyse boundary variation of target cell from the two groups of videos, four statistical parameters were calculated from each of the transformed sub-band coefficients: mean (*M*), variance (*V*), skewness (*S*), and kurtosis (*K*). The skewness is the third-order central moment of the data distribution, which measures whether the distribution of the data is symmetric. This value is zero if the coefficients follow a normal distribution. A large positive or negative skewness value indicates that the coefficient distribution has a relatively long tail on the right or left side, respectively. The kurtosis is a statistic associated with the fourth-order centre moment of the data, and it measures the extent to which the data is concentrated at the centre.

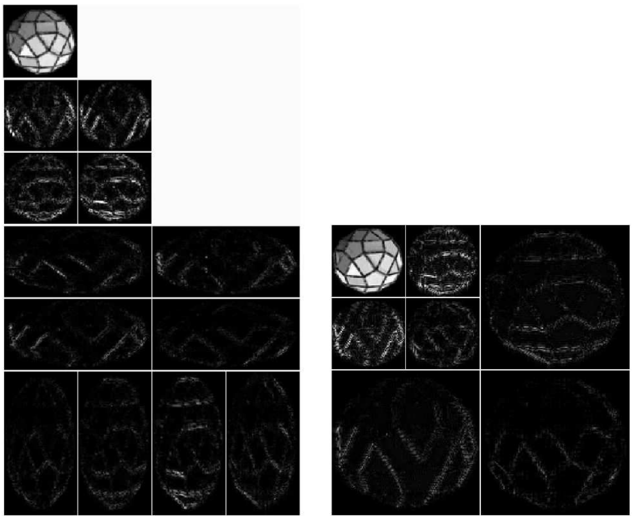
a *b*

Fig. 2 *Coefficient map of Facetscol image after transformation*
(a) Sub-band coefficient map obtained using contourlet transform, ***(b)*** Sub-band coefficient map obtained using wavelet transform

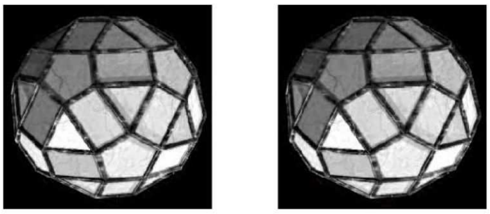
a *b*

Fig. 3 *Original Facetscol image and reconstructed image from contourlet transform coefficient*
(a) Original image, ***(b)*** Reconstructed image

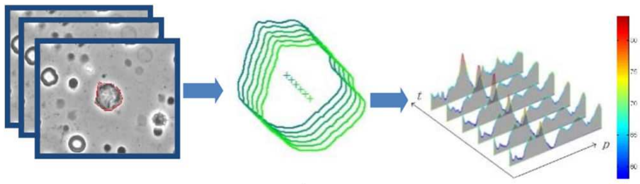

a *b* *c*

Fig. 4 *Process for extracting the edge-to-centroid distance signals from cell boundaries in microscopic video*
(a) Tracking and segmentation of target cell, ***(b)*** Cell boundaries, ***(c)*** The edge-to-centroid distance signals

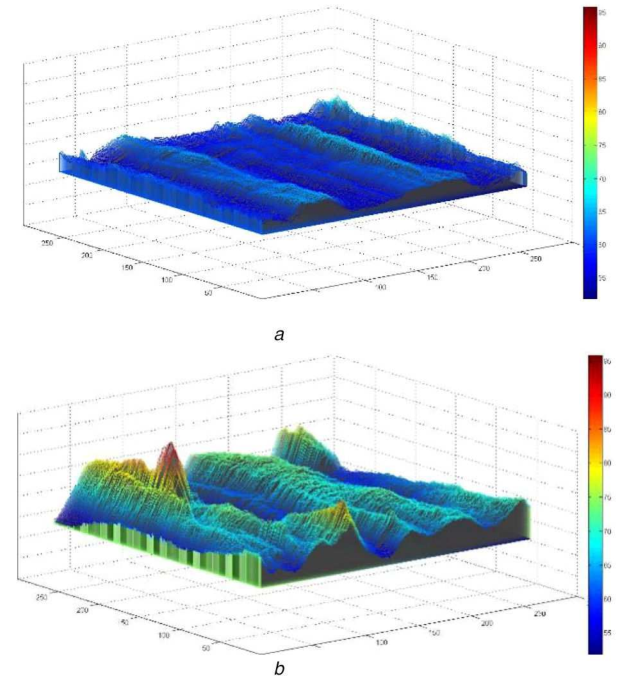

Fig. 5 *Visualisation for edge-to-centre distance signals of cell boundaries in microscopic video*
(a) SST, ***(b)*** AST

Finally, the feature vector was composed of the statistical parameters, representing cell deformation, which was used as the input of neural network for classification of the two kinds of videos.

3 Results

3.1 Visualisation of the edge-to-centroid distance signals

The edge-to-centroid distance signals from the SST group and AST group are shown in Figs. 5*a* and *b*, respectively. It can be seen that the boundary of the target cell changes smoothly in the SST group (similar to a calm sea surface), whereas the boundary of the target cell changes drastically in the AST group (similar to a turbulent sea surface).

3.2 Wavelet and contourlet transform of the edge-to-centroid distance signals

To obtain the boundary variation features of the target cell, further analysis is performed on the edge-to-centroid distance signals. Specifically, the wavelet and contourlet transformation was performed on the edge-to-centroid distance signals $r(p, t)$.

The coefficients map of the wavelet transform performed on the edge-to-centroid distance signals is shown in Fig. 6. These coefficients in the horizontal and vertical represent the variation of $r(p, t)$ along the time and spatial axes, respectively. The variation along the time axis indicates the change of a certain point on the cell boundary over time, whereas the spatial axis reflects the change of the cell boundary in a single frame. The transformation domain coefficients associated with the lighter regions in the image indicate a relatively dramatic variation of cell boundary and vice versa.

The coefficients map of the contourlet transform performed on the edge-to-centroid distance signals is shown in Fig. 7. It can be seen that the signals $r(p, t)$ are decomposed at two different scales. At the coarser scale, the signals are decomposed into sub-bands in four directions. At the finer scale, the signals are further decomposed into sub-bands in eight directions. The characteristics of the target cell boundary variation in different directions at different scales are reflected by the coefficients of each sub-band pointing to distinctive directions.

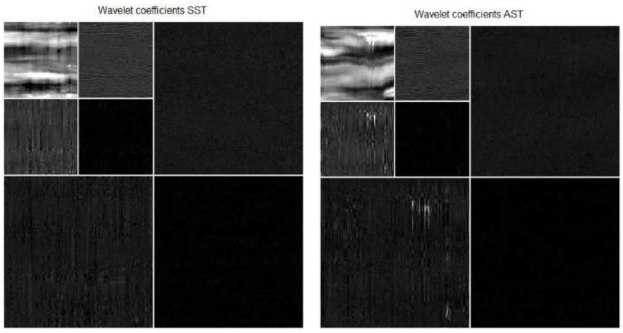

Fig. 6 *Wavelet transform coefficient of edge-to-centroid distance signal for cell in video*
(a) SST group, ***(b)*** AST group

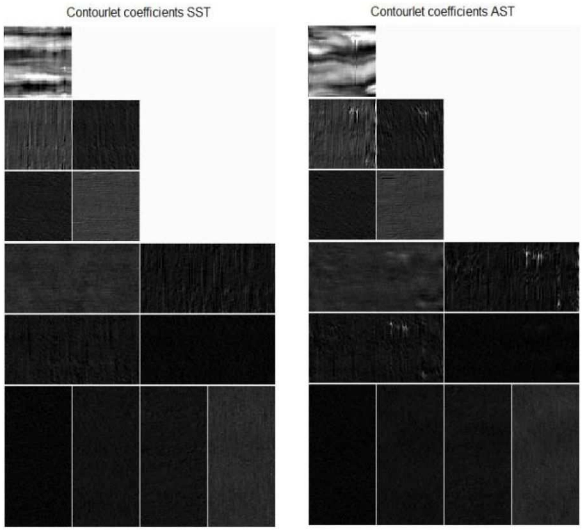

Fig. 7 *Contourlet transform coefficient map of edge-to-centroid distance signals of the target cell*
(a) SST group, ***(b)*** AST group

In Fig. 7, the darker colour in the image corresponds to smaller transformed domain coefficients, whereas the lighter colour corresponds to larger transformed domain coefficients. In the decomposed sub-band, the smaller transform coefficients represent the smooth regions of the image, whereas the larger transform coefficients represent local singular features (dramatic deformation) in specific directions and at specific spatial locations such as edges and contours.

Comparing these coefficients with the results of the wavelet transforms, it can be established that the contourlet transform provides transformed coefficients in a greater number of sub-band directions, reflecting cell boundary variation in more directions in addition to the three basic directions.

3.3 Statistical analysis of the transformed coefficients

To quantitatively analyse the transformed coefficients of the wavelets and contourlets, statistical parameters including M, V, S, and K were calculated, which are shown in a box diagram in Figs. 8–11. Since there is no significant difference in M and S, only the box diagrams of V and K are given here. The horizontal axis indicates whether the data are associated with the SST or AST group. The vertical axis represents statistical parameters. For example, V_{mn} represents the variance of the nth sub-band coefficients obtained by decomposition at the mth scale. The red horizontal line shown in the box diagram represents the median line. The lower and upper sides of the box represent the values associated with 25 and 75% of the samples, respectively. The red cross shown in the top region of the box represents the singularities.

The box diagram provides a direct visualisation of the validity of the statistical parameters calculated for the directional coefficients in each sub-band in the transformation domain. It can be seen from Figs. 8 and 9 that V_{11}, V_{12}, V_{21}, and V_{22} of wavelet

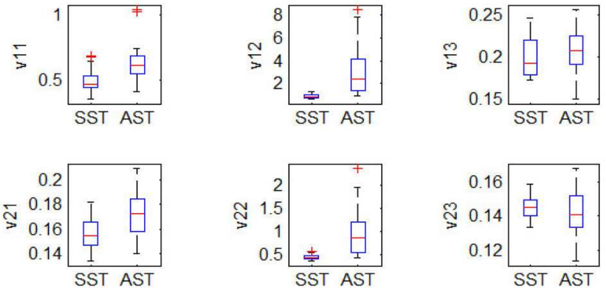

Fig. 8 *Box diagram showing variance of coefficients obtained by wavelet transform*

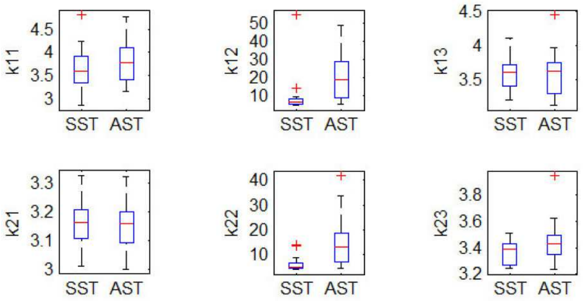

Fig. 9 *Box diagram showing kurtosis of coefficients obtained by wavelet transform*

transform obtained from the SST group are smaller than those of the AST group, which is consistent with the observation that the lymphocyte shape is stable in the SST group, and the deformation is slight. K_{12} and K_{22} from the SST group are also smaller than those from the AST group, which indicates that the distribution of the edge-to-centroid distance signals of the SST group is more concentrated than that of the AST group.

For contourlet transform, as shown in Figs. 10 and 11, V and K obtained from the two groups have the same trend with those of wavelet transform: both V and K in the SST are smaller than those in the AST group. These findings agree with the clinical observations that the shape of the lymphocytes is stable and the deformation is slight in the SST group. Meanwhile, the lymphocytes are more active, and the deformation is intense in the AST group.

To further extract effective quantitative statistical parameters from the coefficients in each sub-band in the transformation domain, statistical analysis was performed on the coefficients in each sub-band. Since the coefficients do not conform to the normal distribution, rank-sum tests were conducted on different samples in different groups. The significance level was set to 0.01. The rank-sum test results are shown in Tables 1 and 2.

It can be seen that V_{11}, V_{12}, V_{21}, V_{22}, K_{12}, and K_{22} from wavelet transform, and V_{11}, V_{12}, V_{13}, V_{21}, V_{22}, V_{23}, V_{28}, K_{11}, K_{12}, K_{22}, K_{23}, and K_{26} from the contourlet transform exhibit significant differences between the two groups. The rank-sum test on the statistical parameters from the contourlet transform yielded a relatively smaller and more stable p-value. In contrast, for the coefficients obtained by the wavelet transform, the rank-sum test yielded a relatively larger p-value.

In this study, a support vector machine (SVM) is used to classify cell morphology in the microscopic video. According to the result of Wilcoxon rank sum tests, the statistical parameters which possess the smaller p-values between the two test groups were combined as a feature vector representing the changes of cell deformation and then fed into the SVM. For each trial, we randomly choose 30 (15 from SST and 15 from AST) as train set and another 10 (5 from SST and 5 from AST) for the test set. We repeated the above procedure 1000 times, the averaged class recognition rate reaches 96.67% for the contourlet transform. In contrast, the averaged recognition rate is 69.67% for the wavelet transform.

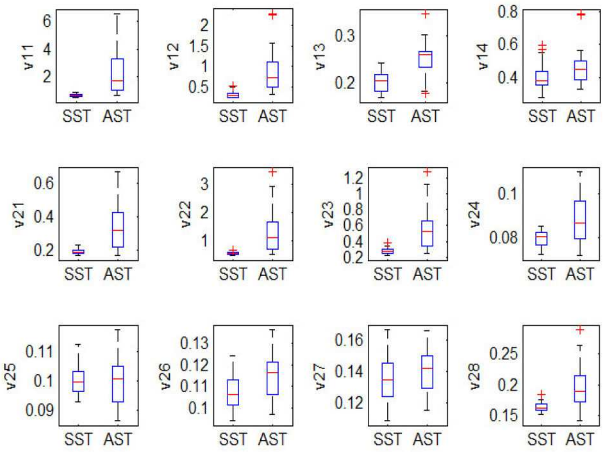

Fig. 10 *Box diagram showing variance of coefficients obtained by contourlet transform*

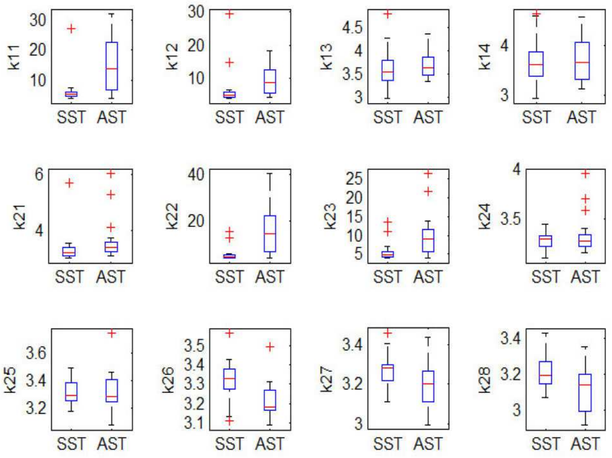

Fig. 11 *Box diagram showing kurtosis of coefficients obtained by contourlet transform*

4 Discussions and conclusions

To characterise the boundary changes of the target cell in a microscopic video, a multi-scale geometric analysis scheme based on the contourlet transform was proposed in this study. First, the edge-to-centroid distance signals of the target cell were calculated from cell boundaries. Second, the contourlet transform was performed on the edge-to-centroid distance signals to obtain the transformed coefficients that represent the singular features in the original surface signal. The larger coefficients in the transformation domain represent the local dramatic change of cell boundary and vice versa. Third, we calculated statistical parameters (including M, V, S, and K) from the transformed coefficients in each sub-band, which represented the boundary change features of the target cell. Finally, the statistical parameters which possess the smaller p-values between the two test groups (evaluated using the rank-sum test) were combined to form the feature vector; then the feature vector was fed to SVM for classification of the two kinds of group data. Meanwhile, for comparison, the above experiment process was repeated using the wavelet transform.

The results of the rank-sum test imply that relatively smaller and more stable p-values were obtained based on the contourlet transform than those with the wavelet transform, which indicates that the contourlet transform captures the characteristic parameters of the target cell boundaries more effectively, owing to its multi-scale and multi-directional decomposition for images with a small redundancy factor.

The results of SVM demonstrate that when using the feature vector from the contourlet transform coefficients, the averaged class recognition rate is higher than that of the feature vector from the wavelet transform coefficients. Our finding is consistent with previous reports that contourlet transform has better performance

Table 1 Wilcoxon rank-sum test results of characteristic parameters associated with sub-band coefficients calculated by wavelet transform from the two types of data

	P	*H*		*P*	*H*
v11	0.0023	1	k11	0.3793	0
v12	9.1266×10^{-07}	1	k12	0.0001	1
v13	0.1806	0	k13	0.9031	0
v21	0.0066	1	k21	0.6949	0
v22	7.5774×10^{-06}	1	k22	0.0001	1
v23	0.3104	0	k23	0.1136	0

Note: $H = 1$ indicates that there is a significant difference between the two types of data when the significance level is 0.01.

Table 2 Wilcoxon rank-sum test results of characteristic parameters associated with sub-band coefficients calculated by contourlet transform from the two types of data

	P	*H*		*P*	*H*
v11	1.5757×10^{-06}	1	k11	0.0001	1
v12	9.1266×10^{-07}	1	k12	0.0016	1
v13	0.0001	1	k13	0.2184	0
v14	0.0385	0	k14	0.7557	0
v21	4.1658×10^{-05}	1	k21	0.0114	0
v22	3.9874×10^{-06}	1	k22	0.0001	1
v23	2.0407×10^{-05}	1	k23	0.0016	1
v24	0.0133	0	k24	0.9461	0
v25	0.9676	0	k25	0.9676	0
v26	0.0411	0	k26	0.0010	1
v27	0.0810	0	k27	0.0114	0
v28	0.0006	1	k28	0.0337	0

Note: $H = 1$ indicates that there is a significant difference between the two types of data when the significance level is 0.01.

in representing the image salient features such as edges, lines, curves, and contours than wavelets for its anisotropy and directionality, therefore well suited for analysing contour change features of the cell boundary.

Finally, this study also has certain limitations. Our effort was motivated by clinicians' observations that lymphocytes in the human peripheral blood exhibit more morphological changes during graft rejection in patients with liver transplants than those of the healthy. Since it was unsafe to conduct experiments on patients with graft rejection, our experiment used mice and considered skin transplants rather than liver transplants. In the future, we will consider expanding the size of the experimental sample to verify the reliability of the algorithm, and further applying the proposed method to cell morphology analysis of patients.

In summary, we have proposed a novel scheme for quantitative analysis of cell morphology-based on contourlet transform in the microscopic video. The experimental results show that the proposed method is superior to that of the wavelet transform in terms of delineating cell boundary variation. Our findings demonstrate that the contourlet transform is effective to display a smooth contour, in addition to lines and surfaces in an image. The effectiveness of the contourlet transform in contributing to an accurate quantitative analysis of cell boundary changes may open a new avenue for cellular morphology analysis in clinical trial research.

5 Acknowledgments

This work was supported by the National Natural Science Foundation of China (11771115 and 11271106), the Youth Foundation of Hebei Province Educational Department (QN2016169), the Scientific Research Foundation for the Returned Overseas Chinese Scholars in Hebei Province (606999919029), the Advanced Talents Incubation Program of Hebei University (801260201075 and 521000981327), and the Post-doctoral Research Foundation of Hebei University. The authors would like to thank the previous president of Beijing You'an Hospital, Ning Li, for providing the microscopic cell images.

6 References

[1] Swedlow, J.R.: 'Advanced hardware and software tools for fast multidimensional imaging of living cells', *Proc. Natl. Acad. Sci. USA*, 2010, **107**, (37), pp. 16005–16006

[2] Biname, F., Pawlak, G., Roux, P., *et al.*: 'What makes cells move: requirements and obstacles for spontaneous cell motility', *Mol. BioSyst.*, 2010, **6**, (4), pp. 648–661

[3] Xiong, Y., Iglesias, P.A.: 'Tools for analyzing cell shape changes during chemotaxis', *Integr. Biol.*, 2010, **2**, (11–12), pp. 561–567

[4] Vermolen, F.J., Gefen, A.: 'A phenomenological model for chemico-mechanically induced cell shape changes during migration and cell–cell contacts', *Biomech. Model. Mechanobiol.*, 2013, **12**, (2), pp. 301–323

[5] Lin, J.-A., Wu, C.-H., Fang, S.-C., *et al.*: 'Combining the observation of cell morphology with the evaluation of key inflammatory mediators to assess the anti-inflammatory effects of geranyl flavonoid derivatives in breadfruit', *Food Chem.*, 2012, **132**, (4), pp. 2118–2125

[6] Ryan, G.L., Watanabe, N., Vavylonis, D.: 'Image analysis tools to quantify cell shape and protein dynamics near the leading edge', *Cell Struct. Funct.*, 2013, **38**, (1), pp. 1–7

[7] Lin, W., Suo, Y., Deng, Y., *et al.*: 'Morphological change of CD4 + T cell during contact with DC modulates T-cell activation by accumulation of F-actin in the immunology synapse', *BMC Immunol.*, 2015, **16**, (1), p. 49

[8] Nassiri, I., McCall, M.N.: 'Systematic exploration of cell morphological phenotypes associated with a transcriptomic query', *Nucleic Acids Res.*, 2018, **46**, (19), pp. e116–e116

[9] Liao, T.T., Wang, L., Jia, R.W., *et al.*: 'Lipophilic organic pollutants induce changes in phospholipid and membrane protein composition leading to vero cell morphological change', *J. Env. Sci. Health B*, 2014, **49**, (10), pp. 760–768

[10] Koslover, E.F., Chan, C.K., Theriot, J.A.: 'Cytoplasmic flow and mixing due to deformation of motile cells', *Biophys. J.*, 2017, **113**, (9), pp. 2077–2087

[11] Maskarinec, S.A., Franck, C., Tirrell, D.A., *et al.*: 'Quantifying cellular traction forces in three dimensions', *Proc. Natl. Acad. Sci. USA*, 2009, **106**, (52), pp. 22108–22113

[12] Paluch, E., Heisenberg, C.P.: 'Biology and physics of cell shape changes in development', *Curr. Biol.*, 2009, **19**, (17), pp. R790–R799

[13] Nazlibilek, S., Karacor, D., Ercan, T., *et al.*: 'Automatic segmentation, counting, size determination and classification of white blood cells', *Measurement*, 2014, **55**, pp. 58–65

[14] Chen, S., Zhao, M., Wu, G., *et al.*: 'Recent advances in morphological cell image analysis', *Comput. Math. Methods Med.*, 2012, **2012**, pp. 1–10

[15] An, X., Liu, Z., Shi, Y., *et al.*: 'Modeling dynamic cellular morphology in images', in Ayache, N., Delingette, H., Golland, P., et al. (Eds.): '*Medical image computing and computer-assisted intervention – MICCAI 2012*' (Springer, Berlin, Heidelberg, 2012), pp. 340–347

[16] Huang, Y., Liu, Z., Shi, Y.: 'Quantitative analysis of live lymphocytes morphology and intracellular motion in microscopic images', *Biomed. Signal Process. Control*, 2015, **18**, (2015), pp. 195–203

[17] Daubechies, I.: '*Ten lectures on wavelets*' (SIAM, Beijing, China, 1992)

[18] Candès, E.J., Donoho, D.L.: 'Ridgelets: A key to higher-dimensional intermittency', *Philos. Trans. R. Soc. Lond. A, Math. Phys. Eng. Sci.*, 1999, **357**, (1760), pp. 2495–2509

[19] Do, M.N., Vetterli, M.: 'The contourlet transform: an efficient directional multiresolution image representation', *IEEE Trans. Image Process.*, 2005, **14**, (12), pp. 2091–2106

[20] Guo, Q., Dong, F., Sun, S., *et al.*: 'Image denoising algorithm based on contourlet transform for optical coherence tomography heart tube image', *IET Image Process.*, 2013, **7**, (5), pp. 442–450

[21] Wang, X., Chen, W., Gao, J., *et al.*: 'Hybrid image denoising method based on non-subsampled contourlet transform and bandelet transform', *IET Image Process.*, 2017, **12**, (5), pp. 778–784

[22] Das, D.K., Koley, S., Bose, S., *et al.*: 'Computer aided tool for automatic detection and delineation of nucleus from oral histopathology images for OSCC screening', *Appl. Soft Comput.*, 2019, **83**, p. 105642

[23] Asmare, M.H., Asirvadam, V.S., Hani, A.F.M.: 'Image enhancement based on contourlet transform', *Signal Image Video Process.*, 2015, **9**, (7), pp. 1679–1690

[24] Darwish, S.M.: 'Multi-level fuzzy contourlet-based image fusion for medical applications', *IET Image Process.*, 2013, **7**, (7), pp. 694–700

[25] Lv, W., Wang, Y., Chen, X., *et al.*: 'Enhancing vascular visualization in laser speckle contrast imaging of blood flow using multi-focus image fusion', *J. Biophotonics*, 2019, **12**, (1), p. e201800100

[26] Wang, H., Shi, J.: 'SAR image segmentation algorithm based on contourlet domain AFMRF model', *IET Image Process.*, 2018, **12**, (7), pp. 1124–1130

[27] Sathya, N., Karuppasamy, K., Suresh, P.: 'Contourlet transform and morphological reconstruction based retinal blood vessel segmentation', *Int. J. Biomed. Eng. Technol.*, 2017, **25**, (2–4), pp. 105–119

[28] Abkenar, M.R., Sadreazami, H., Ahmad, M.O.: 'Salient region detection using feature extraction in the non-subsampled contourlet domain', *IET Image Process.*, 2018, **12**, (12), pp. 2275–2282

[29] Huang, Y., Liu, Z.: 'Segmentation and tracking of lymphocytes based on modified active contour models in phase contrast microscopy images', *Comput. Math. Methods Med.*, 2015, **2015**, Article ID 693484

[30] Candès, E.J.: 'Harmonic analysis of neural networks', *Appl. Comput. Harmon. Anal.*, 1999, **6**, (2), pp. 197–218

[31] Starck, J.L., Candes, E.J., Donoho, D.L.: 'The curvelet transform for image denoising', *IEEE Trans. Image Process.*, 2002, **11**, (6), pp. 670–684

[32] Zhang, G., Lin, Y.: '*Lecture notes on functional analysis*' (Peking University Press, Philadelphia, Pennsylvania, USA., 1987, 1st edn.)